activities, measured electrophysiologically by multifocal ERG *(13)*. Multifocal ERG (VERIS, EDI, San Mateo, California) measures the local neuronal activity in multiple small regions in the posterior retina, when presented (on a TV monitor) with achromatic flicker which alternates independently between black and white in individual hexagonal segments *(25)*. The correlation was evaluated between the amplitudes of the focal ERG responses and optical signals at the corresponding locations, from the same eye. In order to artificially reduce the function of the photoreceptor layer of the retina, the upper half of the left fundus of a monkey was locally coagulated with Argon Laser photocoagulation (**Fig. 6.5A**). The electrophysiological responses in the damaged region were reduced accordingly (**Fig. 6.5B**). In intrinsic signal imaging, the damaged region also showed smaller amount of light reflectance decrease (**Fig. 6.5C**). The light reflectance decrease and the multifocal ERG signal showed statistically significant positive correlation ($r^2 = 0.79$, $p < 0.001$, $n = 45$) (**Fig. 6.5D**). The

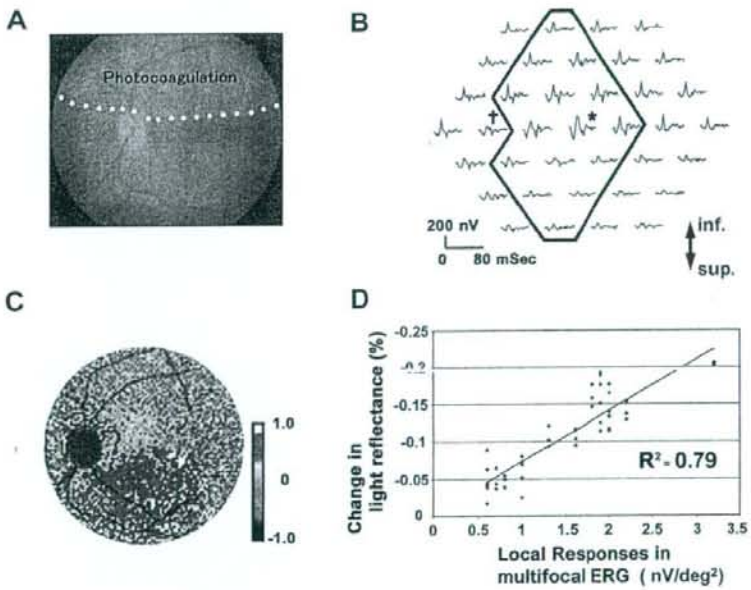

Fig. 6.5. (**A**) Photograph of the monkey's retina artificially damaged by Argon Laser Photocoagulation. The upper half of posterior retina was densely coagulated, sparing the macular area. (**B**) Array of 37 local responses of multifocal ERG, taken from the fundus in (**A**). ERGs with * and † indicate the location of macula and optic disk, respectively. Note that the responses of the intact retina in the lower half region are inversely shown in the upper half of the arrays. (**C**) pseudocolor map of flash-evoked intrinsic signals measured with infrared light. Red color indicates light reflectance decrease (*darkening*) from pre-stimulus level. Flash-evoked darkening could not be observed in the damaged region (*upper half*). (**D**) Correlation between the change in light reflectance decrease and the focal responses in ERG at the corresponding retinal location under infrared light. Correlation coefficient: $r^2 = 0.79$ ($p < 0.001$, n=45). (*See* Color Plate)

results of optical imaging and electrophysiological measurement were well correlated not only in their response amplitudes but also in the spatial location of reduced responses: the border between normal and reduced response regions in both measurements corresponded to the border between normal site and photocoagulation site.

Interestingly, with infrared observation, the time course of the intrinsic signals evoked by a brief flash stimulus was different for different regions of the ocular fundus. Representative time courses of flash-evoked response at the foveal and perifoveal regions under the dark-adapted condition are shown in **Fig. 6.6**. The reflectance changes at the fovea were rapid and reached a negative peak (darkening) within 100 to 200 ms following the flash. The darkening then gradually returned toward the pre-stimulus baseline. The signals in the perifoveal regions (3°–12°) were composed of both fast and slow components. The time courses of the intrinsic signals of the perifoveal regions were approximately the same and distinct from the foveal response: the light reflectance decreased rapidly within 100 ms (flexural point), and then gradually decreased to reach a trough. The light reflectance at the fovea did not decrease following the initial negative peak.

The fovea is a central region (300 μm in diameter) in the posterior retina that is composed of cone photoreceptors and is free of capillaries and middle or inner layer structures *(26)*. The perifoveal region has both cone and rod photoreceptors, and its

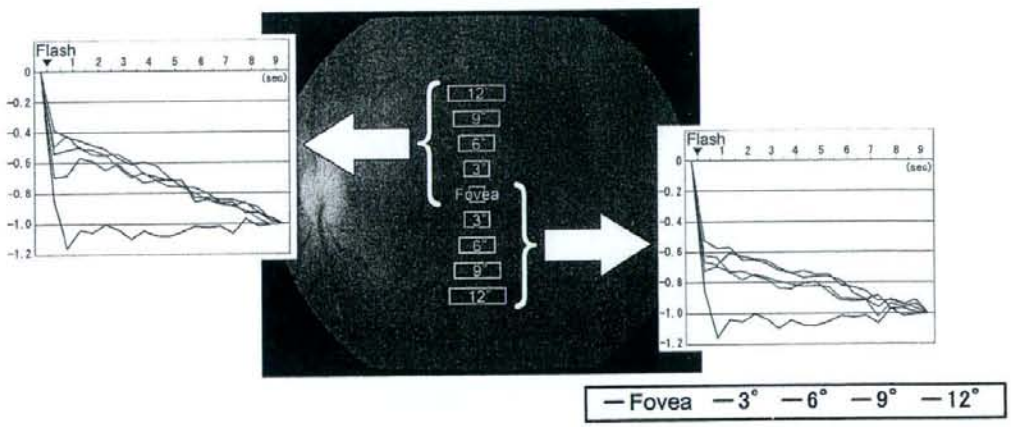

Fig. 6.6. Time courses of light reflectance changes in a single trial following a diffuse flash, measured at the fovea and different regions within twelve degrees superior or inferior to the fovea. Amplitudes are indicated as values relative to the light reflectance changes at the end of each trial (1.0). The four regions tested in each quadrant are indicated as distances from the fovea (3,6,9 and 12°). (*See* Color Plate)

inner and middle layers are nourished by retinal vessels and capillaries. We believe that the light scattering changes following activation of the cone photoreceptors are probably the source of the fast intrinsic signals observed at the fovea because the foveal avascular region is not subject to changes in hemoglobin concentration or blood volume following neural activation *(14)*. The rapid darkening observed at the perifoveal regions may also be derived from light scattering changes because, under infrared light, the change in the optical signal due to deoxygenated hemoglobin concentration is thought to be much smaller than that from tissue light scattering *(27)*. The light scattering changes following a flash are thought to be derived from microstructural changes in the outer segment disks, membrane hyperpolarization, cell swelling, and changes in the composition of the inter-photoreceptor matrix. Recent functional OCT studies using blood-free slice preparations *(28,29)* or in vivo retina *(30)* showed that the reflectance in the photoreceptor layer is strongly modulated by neural activation followed by microscopic morphological changes.

As for the sources of the slow signals in the perifoveal regions, our recent studies have suggested that the light scattering changes due to blood flow changes in capillaries are the main contributors to changes in reflectance *(42)*. Direct measurement of blood flow with laser Doppler flowmetry has shown that a flash stimulus evokes a slow increase in blood flow only in the perifoveal regions and its time course exactly matched that of the slow component of the intrinsic signals we described above. A fast increase in blood flow, however, has not been observed either in foveal or perifoveal regions.

We have shown that the light scattering change, which is independent of blood oxygenation level, also correlates well with neuronal activity and can be used for mapping neural function. We believe that this fast scattering signal is of great value for mapping neuronal activity because it may have better spatial and temporal resolutions than the blood-flow- or blood oxygenation related signals.

3. Optical Coherence Tomography (OCT) for Functional Imaging Resolved in Depth (Functional OCT)

In conventional OISI with CCD cameras, the measured reflected light is actually the integrated signals over depths determined by the collection optics. Hence potential variations in functional organization across depth may go undetected. Optical coherence tomography (OCT) is an optical imaging technique that has the potential to show reflectivity at specific depths because the method is a sensitive measure of refractive index variations across

depth *(31,32)*. In this technique, light from a low-coherence light source is focused onto the tissue and reflectivity of the internal microstructures at different depths is measured by an interferometer, thus providing a map of the structural profile of the tissue. As described in the previous section on conventional OISI, in addition to the oxy- and deoxy-hemoglobin related absorption changes, scattering changes also contribute to the intrinsic signal measured with OCT. Scattering changes could result from changes in the size of the scatterer or the density of the scatterer, or both. During neural activation, secondary physiological structural changes such as those in photoreceptors described above *(13)*, capillary dilation *(12,33)*, change in the density of red blood cells *(34)* and swelling of glial cells *(35)* can occur *(36)*. We expect that the changes in scattering characteristics would result in an activity-dependent reflectivity change, and that the sensitivity of OCT to refractive index changes would make it theoretically sensitive to the scattering changes such as those happening during neural activation. We refer to this technique as functional OCT (fOCT) and its signal as fOCT signal.

To demonstrate the potential of OCT in functional studies, we used primary visual cortex (V1) of cats to confirm that detection of a stimulus-specific reflectivity change is feasible *(36, 37)*. The reliability of the technique was demonstrated by comparison with results of conventional OSIS and multi-unit activity recorded electrophysiologically. Recently, supporting evidence for the potential of OCT in functional studies has been reported in squid *(38)* and in retina *(28–30)*.

4. Brief Introduction for Optical Coherence Tomography (OCT)

Figure 6.7A shows a simple schematic of the principles of an interferometer: a broad-spectrum light source is divided by a half mirror into two beams, one illuminating the reference mirror and the other illuminating a turbid medium such as the cortex. The light reflected back from the reference mirror and the cortex are recombined at the half mirror to reach the detector. The reflected light beams would interfere only if their total light path length difference (Lr-Ls) is within the coherence length of the source, or, in other words, if the light reaching the detector has temporal correlation. The extent of temporal correlation is determined by autocorrelation of the source, and can be described in terms of the spectral width (Proportional to $\lambda_0^2/\Delta\lambda$) of the source, where λ_0 is the central mean wavelength and $\Delta\lambda$ the spectral width. For the case of the light source used in OCT, the coherence length is on the order of a few μm to a few tens of μm. So, by having a mechanism to move the reference mirror, it is possible to dissect

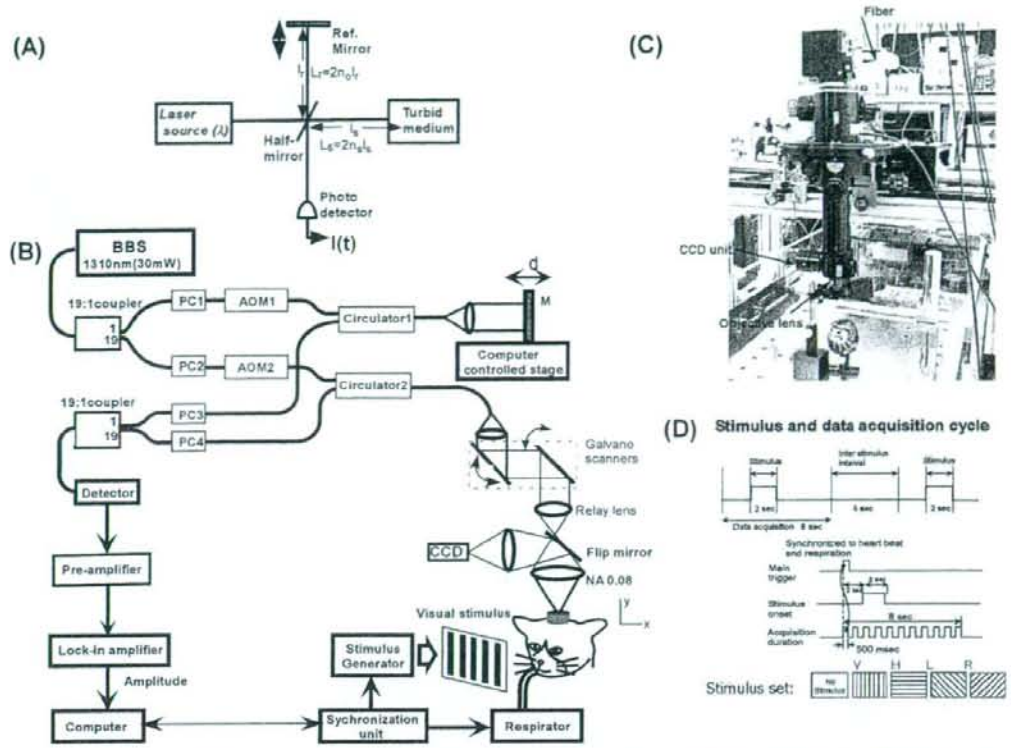

Fig. 6.7. A schematic of the basic principle of OCT (**A**) and the experimental system used (**B**) along with a picture of the probe unit (**C**) and a schematic of the scanning paradigm (**D**). In the figure (**B**), the abbreviations denote: BBS - Broad Band Source, AOM- Acousto-Optic Modulator, PC - Polarization Controller, M – Mirror and O – Objective lens. (*See* Color Plate)

the cortex optically and obtain depth-resolved reflectivity maps. The experimental system used in our studies and other details are described in Appendix 2.

5. Functional Imaging with OCT (fOCT)

Prior to doing functional imaging with OCT, we performed in vivo optical intrinsic signal imaging with the exposed cortical surface of cat visual cortex (**Fig. 6.8A**) at a wavelength of 607 nm. The stimulus set was identical to the one used in fOCT. It consisted of four differently oriented gratings and a blank screen used as a control (see detailed protocol in Appendix 2). **Figure 6.8B** shows the thresholded difference maps obtained when horizontal and vertical grating visual stimuli were presented to the cat. Dark and bright regions indicate the activated regions for horizontal and vertical gratings, respectively.

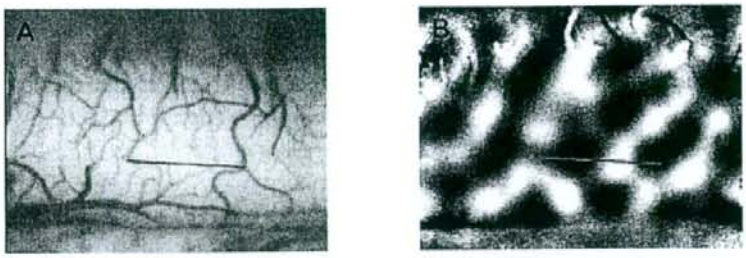

Fig. 6.8. (**A**) Exposed cortical surface of cat visual cortex with (**B**) a thresholded activation map overlay . *Dark* and *light* patches represent the activated regions for horizontal and vertical gratings, respectively, and *green lines* indicate the region of OCT scans. (*See* Color Plate)

An OCT x-z scan was then conducted across the green line indicated in **Figure 6.8**. **Figure 6.9A** shows the results of the OCT structural x-z image obtained. The cortical surface border has been drawn manually and the warm-colored regions indicate the scattering centers within the cortex. Here, the light beam was adjusted to be incident normal to the cortical surface and at a position of interest in relation to the cortical surface. The depth profile showing the intensity variation as a function of depth is shown in **Fig. 6.9B**. **Figure 6.9C** shows the calculated fOCT map obtained as a difference of the fOCT maps collected for horizontal and vertical grating stimuli obtained across the green line of **Fig. 6.8** (see Appendix 2 for calculation used to extract

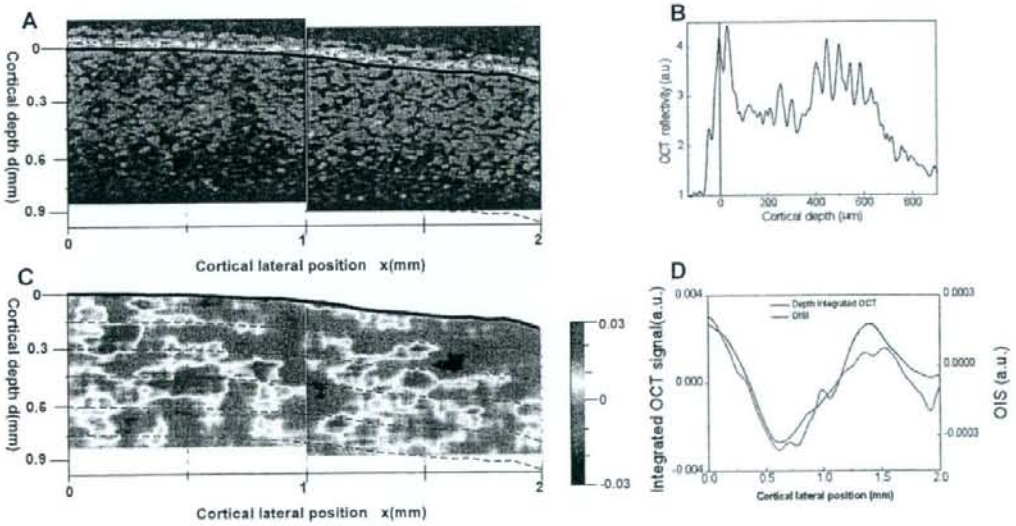

Fig. 6.9. (**A**) OCT scan obtained across the line indicated in Fig. 6.8 with (**B**) a typical depth reflectivity profile from (**A**) and the corresponding (**C**) Functional OCT map and (**D**) Consistency of OISI result with the integrated result of fOCT. In (**C**), *red* and *blue* patches represent the activated regions for horizontal and vertical gratings, respectively. In (**D**) green line indicates the variation of OISI across the line indicated in Fig. 6.8B. while the *red line* obtained by calculating the functional signal from integrating the OCT scans across the full scanned depth range of Fig. 6.9A. (*see* Color Plate)

functional signals). Here, red and blue patches indicate the activation for horizontal and vertical grating stimuli, respectively. In order to clarify the reliability of maps, a pixel-by-pixel comparative t-test was done for the horizontal against the vertical grating stimuli. The tests revealed that the results obtained were statistically significant to within a 5% tolerance limit. Further, a blank minus blank map did reveal a flat distribution without any patches.

From the fOCT map, we can make the following inferences:

1. There is a discrete distribution of activation patches across depth, which is stimulus specific.
2. In a very superficial region (100–200 μm under cortical surface), there are no activation patches indicating layer 1 where neurons are scarce.
3. In the region deeper than 100–200 μm, there exist several localized patches across depth showing no regular structure.
4. The localized patches extend up to the measured depth of approximately 1 mm. The presence of orientation columns in primary visual cortex is well known *(39)*. This indicates that, across depth, there might exist a continuous cylindrical organization more complex than the commonly understood columnar organization.

As the maps revealed by fOCT suggest a surprisingly discrete distributed columnar organization, it becomes necessary to validate the technique. In the present measurements, there are two potential issues that need to be considered:

1. Although we could observe a functional signal that arises as a result of scattering change due to neural activation, it is still not possible to specify the origin regarding the exact nature of the scattering changes such as glial swelling or capillary dilation. One way to resolve this issue may be to increase the spatial resolution of the technique, a possibility that is technically feasible. But even with increased resolution, allowing us to visualize the details of the structural organization, it is still not clear whether the reflectivity changes could provide enough contrast to resolve finer details such as neuronal cells, glial cells and blood vessels etc. To resolve such structural differences, one way is by specifically attaching contrast agents such as gold particles to specific structures such as neurons. We previously proposed a method of increasing the reflectivity in OCT *(40)* by introducing properly sized gold particles. With such specific labeling, we may be able to increase the reflectivity from specific structures, which would, in turn, enable us to specify the origin of scattering change.
2. Another issue is that the site of localized scattering change may not correspond to the site of neural activity. To address this problem, we conducted electrophysiology recordings to measure the neuronal activity at the sites revealed by fOCT discussed in the following section.

6. Reliability of the Signal as a Measure of Localization of Neural Activity

As the correlation of OISI maps with neural activity is already well established *(3, 4, 41)*, a comparison of fOCT with OISI is a reasonable validation approach. We compared the intensity variation of an OISI map across the scanned line (**Fig. 6.8**) with the integrated profile of fOCT. In order to calculate the integrated profile, all the pixels across the z-direction were summed to obtain a profile that varies only across x; then the differential OCT at each x was calculated. **Figure 6.9D** shows the result of such a comparison with the red line indicating the integrated result and green line indicating the OIS intensity variation. A clear and remarkable agreement between the profiles can be seen. This indicates that fOCT signal is indeed correlated with OISI and thus correlated with the neural activity. Experiments were done in 5 cats and showed a good correlation between the integrated fOCT signal and the intensity profiles obtained from intrinsic maps. Correlation coefficients vary in the range of 0.3–0.9. **Table 6.1** gives the results of correlation coefficients obtained from a cat from different scan positions. However, a general caveat is that there are many differences between OISI and fOCT, including illumination and detection geometries, wavelengths used and the origin of the signals. In fOCT, as near-infrared wavelength is used, oxy- and deoxy-hemoglobin have almost the same absorption coefficients and hence the absorption changes are minimal. The main source of the signal is thought to be scattering changes. Nevertheless, the OISI results corresponded very well with the integrated profiles of fOCT.

Table 6.1
The correlation coefficients between the profiles obtained by the OISI intensity profile and the corresponding depth-integrated fOCT intensity profile obtained from 6 different scan positions of a single cat

Scan position index	Correlation for 0–90°	Correlation for 45–135°
Position 1	0.58	0.65
Position 2	0.32	0.29
Position 3	0.24	0.39
Position 4	0.89	0.77
Position 5	0.407	0.539
Position 6	0.566	0.559

Next, to investigate what the patches in fOCT maps represent (i.e., whether they represent a localization in the distribution of neurons themselves or a localization of the secondary mechanisms that are behind the origin of the functional signals), we recorded multi-unit activities (MUA) in the scanned region to determine the correlation with the distribution of strength of neuronal activity. MUA recordings were done with glass-coated tungsten electrodes. **Figure 6.10A** shows a representative example of the variation of MUA with respect to the cortical depth for four different grating orientations. As seen from the figure, the stimulus selectivity across a single track is retained. However, the evoked response at different depths is not of the same magnitude and it varies across depth with the response being the largest for a depth of 100–400 μm. This implies that, across the depth, all neurons do not behave in the same way and they have individual characteristics as would be expected from an ensemble of neurons. We would like to emphasize this variation in the evoked response and we expect this variation could be detected by the proposed fOCT measurement.

Figure 6.10B shows an example of the result of a comparison of the fOCT depth profile with the MUA profile. Variation of the fOCT profile generally agrees with the non-uniformity of evoked response across different depths. This suggests that the functional signal measured by fOCT may be correlated with the spiking activity of neurons. A calculation of the correlation coefficient revealed that the profiles are well interrelated. Results of correlation obtained from six different scan positions and three different cats are presented in **Table 6.2A and B**, respectively. Except for two cases, the correlation coefficient was fairly high, indicating that fOCT could indeed measure functional maps.

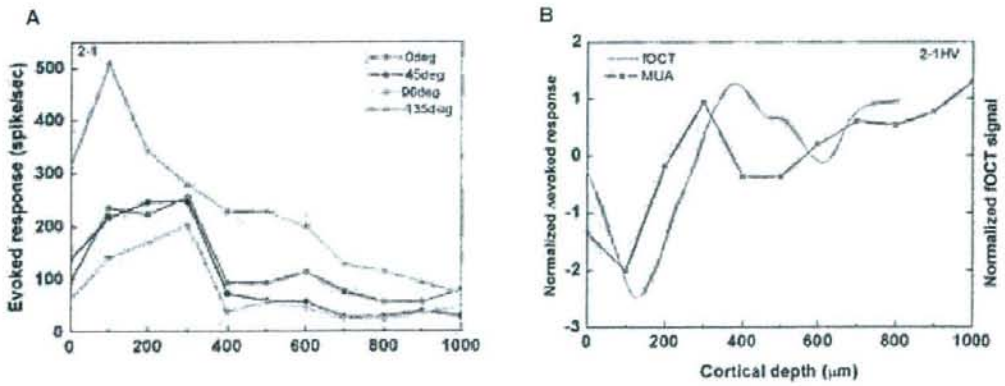

Fig. 6.10. An example of (**A**) MUA-evoked responses as a function of depth obtained from a single track for different orientation stimuli and (**B**) a comparison of difference of the evoked MUA response (shown in red) with the fOCT profile (shown in green) as a function of depth for the difference of 0° minus 90° orientation stimulus. (*See* Color Plate)

Table 6.2
Cross-correlation coefficients obtained from (A) different tracks of a single averaged x–z scan and (B) population result from three different cats

Correlation between fOCT and unit profiles (A)

Site #	Correlation coeff. for 0–90 deg	Correlation coeff. for 45–135
#1	0.94	0.66
#2	0.809	0.764
#3	0.908	0.926
#4	0.852	0.899
#5	0.348	0.374
#6	0.751	0.365
(B)		
Cat #	# of sites that show significant correlation ($p<0.005$)	
C-22	4/8	
C-30	9/11	
C-36	5/11	

7. fOCT – Future Prospects

It should be mentioned that in the comparison study discussed in the previous section, different methods of OISI, fOCT and MUA were conducted independently to be compared later. However, there could be some spatial ambiguity of 100 μm or more in such comparisons. For more reliable comparisons, it may be necessary to conduct simultaneous measurements of OISI, fOCT and MUA. In addition, recently, we have started the implementation of a high speed Fourier domain OCT system that would largely improve the sensitivity of OCT signal enabling a clearer picture of the columnar organization of orientation columns in cat visual cortex.

Recently, we have also started applying fOCT to the study of the rat olfactory system and our preliminary results show clear odor-dependent responses. We therefore expect this method to provide novel insights regarding the response distribution in granule cell layers that receive input from olfactory glomeruli and lie deeper from superficial regions of the bulb.

Appendix 1: Technical Details of Functional Retinography

The monkeys were anesthetized by a mixture of 70% N_2O, 30% O_2 supplemented with 1.0–1.5% of isoflurane and were paralyzed with vecuronium bromide (0.1–0.2 mg/ kg/ hour). Before the recordings, the pupils were fully dilated with topical tropicamide (0.5%) and phenylephrine hydrochloride (0.5%). A modified digital fundus camera system (NM-1000, Nidek, Aichi, Japan) was used to observe and measure the light reflectance changes from the ocular fundus. The fundus images were recorded with a CCD camera (PX-30BC, Primetech Engineering, Tokyo, Japan), and the images were digitized with an IBM/PC-compatible computer equipped with a video frame grabber board (Corona II, Matrox, Quebec, Canada: gray level resolution, 10 bits; spatial resolution, 640 x 480; temporal resolution, 1/30 s). The camera was focused on the macular vessels, and the area recorded covered 45 degrees, which included the macula, superior and inferior vascular arcades, and the optic disk.

The fundus was continuously monitored with light from a halogen lamp filtered through a red (610–650 nm) or infrared (840–900 nm) interference filter. Each recording trial consisted of three hundred video frames collected at 30 frames/sec for a total recording time of 10 s. A Xenon flash (duration: 1 msec) was given to the whole posterior pole of the ocular fundus, 500 msec after the initiation of data acquisition. The flash intensity measured at the cornea was 1.54×10^2 cd•s/m^2. The timing of the data acquisition and stimulus delivery was under computer control. Changes in light reflectance from the ocular fundus following the stimulus, such as a darkening (a decrease in light reflectance) or a brightening (an increase in light reflectance), were measured. The optical signal was calculated as follows: *(1)* The gray-scale values of the image obtained after the stimulus were divided, pixel by pixel, by those obtained during a 0.5-s period before the stimulus, and *(2)* This ratio was rescaled to 256 levels of gray-scale resolution to show the stimulus-induced reflectance changes.

8. Appendix 2: *Technical Details of fOCT*

System

We used a fiber-based OCT imaging system (**Fig. 6.7B**). It consists of a Mach-Zehnder-type heterodyne interferometer

constructed from single-mode fibers for flexibility. Light from a broadband source (AFC Technologies, Canada) operating at an output power of 30 mW and having a central mean wavelength (λ_0) of 1.31 μm and a spectral width ($\Delta\lambda$) of 50 nm is split into sample and reference beams in the respective ratio of 19:1 by coupler 1. Optical frequencies of the sample and reference beams are shifted by acousto-optic modulators (AOM, Asahi glass, Japan). We use AOMs to introduce a constant and stable phase delay between the interfering beams. Both the reference and sample beams, after passing through the circulators, illuminate the reference mirror and cortex, respectively. The reflected lights were recombined at coupler 2. An interference beat signal that has a beat frequency of 250 kHz is detected only when the path lengths of the interferometer arms are matched to within the coherence length of the source that is calculated to be 34 μm in free space. Heterodyne detection was done with a lock-in amplifier (EG&G, USA) and the amplitude of the demodulated components was fed into a computer via a 16-bit A/D converter. The reference mirror M was mounted on a motorized stage and scanned at a speed of 2 mm/sec.

The sample arm viewing the animal side consisted of an objective lens of numerical aperture 0.08 and was also fitted with a CCD camera. This allowed simultaneous viewing of the cortical surface with the introduction of visible light from an auxiliary laser source (wavelength 680 nm). The whole unit was mounted on a manipulator unit (**Fig. 6.7C**) that has five degrees of freedom of translation along three axes and rotation and tilt (the flexibility is needed for making the probing light beam normal to the cortical surface). Galvano scanners were installed so as to perform surface scans. The animal-related fluctuation in the signal was reduced by conducting measurements in synchronization with heartbeat and respiration and by keeping the brain surface immobile using agarose.

Animals and Surgery

Each cat was anesthetized with a mixture of 70% N_2O and 30% O_2 supplemented with 1–2% isoflurane, paralyzed with Pancuronium bromide (0.1 mg/Kg/hr), and artificially ventilated by a respirator unit. Contact lenses were fitted to the eyes to protect the cornea from drying. The pupils of the eyes were dilated with 0.5% tropicamide and 0.5% phenylephrine hydrochloride. The head of the animal was held tightly by attaching it to a metal rod. A stainless steel chamber (18 mm inner diameter) was fixed onto the skull with dental acrylic cement by aseptic surgery and was placed above area 18 (coordinates A10P5 of Horsheley). After removal of the dura mater, the inside of the chamber was

filled with 1.2% agarose (Agarose-HGS, Nacalai tesque, Japan, gel strength 1.5%) containing dexamethasone and antibiotics and was sealed with a round glass cover slip and a silicon gasket. Rectal temperature, ECG and expired CO_2 were continuously monitored during both OCT experiments and surgery.

OCT Scan

The stimuli were the same as that used for OISI and consisted of square-wave gratings (white = 8 cd/m2, black=0 cd/m2) having a spatial frequency and moving at a velocity of 4 degrees/sec. The stimulus set consisted of five patterns with control or blank (mean luminance 4 cd/m^2), horizontal (0°), vertical (90°) and oblique gratings (45°, 135°) and were presented in a random order. All stimuli were generated with a VSG2/3 graphics video board (Cambridge Research Systems, UK). The center of the visual field was roughly estimated by projecting images of optic discs onto a screen in front of the animal. The distance of the CRT screen (200–300 mm) was adjusted to have the best focus of optic discs and surrounding vessel patterns. A total of 40 trials were obtained for each stimulus. In a single trial, data acquisition was done for 8 s, during which time 16 *x-z* frames (128×100 pixels corresponding to 1 × 1 mm) were obtained. The inter-stimulus interval (ISI) was 5 s. A schematic is shown in **Fig. 6.7D**. Stimuli appeared with a delay of 2 s after the acquisition onset and persisted for 2 s.

OCT Data Correction and Analysis

First, the scans were corrected for any misalignment of the surface position by a correlation-based procedure. For a single stimulus, we obtained a total of 640 scans. To compensate for the small variations in the surface position over different scans, we used correlation analysis. Out of these 640 scans, we selected an arbitrary scan (i) with the reflectivity detected as a function of depth being $R_s(x,z,i)$ at a lateral position x for a stimulus s. Next, we calculated the correlation between the ith scan and rest of the scans (j) using the following equation:

EMBED Equation.DSMT4

$$\Omega(\Delta z; i, j) = \frac{\int_{-\infty}^{\infty} R_s(x, z, i) R_s(x, z + \Delta z, j) dz}{\sqrt{\int_{-\infty}^{\infty} R_s(x, z; i) dz \int_{\infty}^{\infty} R_s(x, z + \Delta z; j) dz}} \quad (6.1a)$$

This operation gives the position of the correlation peak that corresponds to the amount of shift necessary for the jth profile to be in alignment with the ith profile.

Pixel noise was removed with a smoothing filter of window size 27 ×21 μm.

Next, the ratio of the post-stimulus over pre-stimulus scans was calculated for all the grating stimuli and the control condition as follows:

$$\gamma_s(x,z,t) = \frac{R_s^{post}(x,z,t)}{\Sigma_{Prescans} R_s^{Pre}(x,z,t)} \quad (6.2)$$

Here R_s is the reflectivity at position (x, z) at time t. "post" and "pre" indicate post-stimulus and pre-stimulus scans. The division operation removes the unchanging common variation and extracts only changes due to visual stimulation. Next, the ratio was averaged for all the scans obtained for each stimulus $< \gamma_s(x,z) >$. Finally, the differential OCT signal $< \gamma_{diff}(x,z) >$ was calculated as,

$$< \gamma_{diff}(x,z) > = < \gamma_{grating}(x,z) > - < \gamma_{control}(x,z) > . \quad (6.3)$$

With the above equation, by subtracting the differential OCT signal of the control, we could remove noise fluctuations such as respiration artifacts that were locked to the recording but not to the grating stimulus . We have restricted this discussion mainly to the results obtained by calculating the difference between $<\gamma_s$ (x,z)> that were obtained for two orthogonal gratings. The spatial map has been smoothed with a moving average filter roughly 100×115 μm.

References

1. Blasdel, G.G. and Salama, G. (1986) Voltage-sensitive dyes reveal a modular organization in monkey striate cortex. *Nature* 321 (6070), 579–585
2. Grinvald, A. et al. (1986) Functional architecture of cortex revealed by optical imaging of intrinsic signals. *Nature* 324 (6095), 361–364.
3. Ts'o, D.Y. et al. (1990) Functional organization of primate visual cortex revealed by high resolution optical imaging. *Science* 249 (4967), 417–420.
4. Bonhoeffer, T. and Grinvald, A. (1991) Iso-orientation domains in cat visual cortex are arranged in pinwheel-like patterns. *Nature* 353 (6343), 429–431.
5. Malonek, D. et al. (1994) Optical imaging reveals the functional architecture of neurons processing shape and motion in owl monkey area MT. *Proc R Soc Lond B Biol Sci* 258 (1352), 109–119.
6. Roe, A.W. and Ts'o, D.Y. (1995) Visual topography in primate V2: Multiple representation across functional stripes. *J Neurosci* 15 (5 Pt 2), 3689–3715.
7. Wang, G. et al. (1998) Functional architecture in monkey inferotemporal cortex revealed by in vivo optical imaging. *Neurosci Res* 32 (1), 33–46
8. Uchida, N. et al. (2000) Odor maps in the mammalian olfactory bulb: Domain organization and odorant structural features. *Nat Neurosci* 3 (10), 1035–1043.
9. Tsunoda, K. et al. (2001) Complex objects are represented in macaque inferotemporal cortex by the combination of feature columns. *Nat Neurosci* 4 (8), 832–838.
10. Vanzetta, I. and Grinvald, A. (1999) Increased cortical oxidative metabolism due to sensory stimulation: Implications for functional brain imaging. *Science* 286 (5444), 1555–1558
11. Vanzetta, I. et al. (2004) Columnar resolution of blood volume and oximetry functional maps in the behaving monkey; implications for FMRI. *Neuron* 42 (5), 843–854

12. Fukuda, M. et al. (2005) Localization of activity-dependent changes in blood volume to submillimeter-scale functional domains in cat visual cortex. *Cereb Cortex* 15 (6), 823–833
13. Tsunoda, K. et al. (2004) Mapping cone- and rod-induced retinal responsiveness in macaque retina by optical imaging. *Invest Ophthalmol Vis Sci* 45 (10), 3820–3826
14. Hanazono, G. et al. (2007) Intrinsic signal imaging in macaque retina reveals different types of flash-induced light reflectance changes of different origins. *Invest Ophthalmol Vis Sci* 48, 2903–2912
15. Bowmaker, J.K. et al. (1980) Microspectrophotometric demonstration of four classes of photoreceptor in an old world primate, Macaca fascicularis. *J Physiol* 298, 131–143
16. Kilbride, P.E. et al. (1983) Determination of human cone pigment density difference spectra in spatially resolved regions of the fovea. *Vision Res* 23 (12), 1341–1350
17. Kilbride, P.E. et al. (1989) Human macular pigment assessed by imaging fundus reflectometry. *Vision Res* 29 (6), 663–674
18. Elsner, A.E. et al. (1993) Mapping cone photopigment optical density. *J Opt Soc Am A* 10 (1), 52–58
19. Mandelbaum, J. and Sloan, L.L. (1947) Peripheral visual acuity. *Am J Ophthalmol* 30, 581–588
20. Birch, D.G. et al. (1987) The relationship between rod perimetric thresholds and full-field rod ERGs in retinitis pigmentosa. *Invest Ophthalmol Vis Sci* 28 (6), 954–965
21. Pulos, E. (1989) Changes in rod sensitivity through adulthood. *Invest Ophthalmol Vis Sci* 30 (8), 1738–1742
22. Osterberg, G. (1935) Topography of the layer of rods and cones in the human retina. *Acta ophthalmol* 13 (Suppl 6), 6–97
23. Curcio, C.A. et al. (1987) Distribution of cones in human and monkey retina: Individual variability and radial asymmetry. *Science* 236 (4801), 579–582
24. Packer, O. et al. (1989) Photoreceptor topography of the retina in the adult pigtail macaque (Macaca nemestrina). *J Comp Neurol* 288 (1), 165–183
25. Sutter, E.E. and Tran, D. (1992) The field topography of ERG components in man – I. The photopic luminance response. *Vision Res* 32 (3), 433–446
26. Weinhaus, R.S. et al. (1995) Comparison of fluorescein angiography with microvascular anatomy of macaque retinas. *Exp Eye Res* 61 (1), 1–16
27. Bonhoeffer, T. and Grinvald, A. (1996) Optical Imaging Based on Intrinsic Signals: The Methodology. In *Brain Mapping* (Toga, A.W. and Mazziotta, J.C., eds.), pp. 55–97, Academic Press, New York
28. Yao, X.C. et al. (2005) Rapid optical coherence tomography and recording functional scattering changes from activated frog retina. *Appl Opt* 44 (11), 2019–2023
29. Bizheva, K. et al. (2006) Optophysiology: depth-resolved probing of retinal physiology with functional ultrahigh-resolution optical coherence tomography. *Proc Natl Acad Sci U S A* 103 (13), 5066–5071
30. Srinivasan, V.J. et al. (2006) In vivo measurement of retinal physiology with high-speed ultrahigh-resolution optical coherence tomography. *Opt Lett* 31 (15), 2308—2310
31. Huang, D. et al. (1991) Optical coherence tomography. *Science* 254 (5035), 1178–1181
32. Bouma, B.E. and Tearney, G.J. (2002) *Handbook of Optical Coherence Tomography*, Marcel Dekker Inc.
33. Malonek, D. et al. (1997) Vascular imprints of neuronal activity: relationships between the dynamics of cortical blood flow, oxygenation, and volume changes following sensory stimulation. *Proc Natl Acad Sci U S A* 94 (26), 14826–14831
34. Tomita, M. et al. (1983) Effects of hemolysis, hematocrit, RBC swelling, and flow rate on light scattering by blood in a 0.26 cm ID transparent tube. *Biorheology* 20 (5), 485–494
35. Holthoff, K. and Witte, O.W. (1998) Intrinsic optical signals in vitro: A tool to measure alterations in extracellular space with two-dimensional resolution. *Brain Res Bull* 47 (6), 649–655
36. Rajagopalan, U.M. et al. (2003) Functional optical coherence tomography to reveal functional architecture of cat visual cortex in vivo. In *Proceedings of SPIE* (Vol. 5140), pp. 77–83
37. Maheswari, R.U. et al. (2003) Novel functional imaging technique from brain surface with optical coherence tomography enabling visualization of depth resolved functional structure in vivo. *J Neurosci Methods* 124 (1), 83–92
38. Lazebnik, M. et al. (2003) Functional optical coherence tomography for detecting neural activity through scattering changes. *Opt Lett* 28 (14), 1218–1220
39. Hubel, D.H. and Wiesel, T.N. (1977) Functional architecture of macaque monkey visual cortex. *Proc R Soc Lond B Biol Sci* (198), 1–59
40. Rajagopalan, U.M. et al. (1999) An optical coherence tomographic imaging system for investigating cortical functional

organization of brain: A simulation study. In *The International Society for Optical Engineering* (Vol. 3749), pp. 400–401
41. Bonhoeffer, T. and Grinvald, A. (1993) Optical imaging of the functional architecture in cat visual cortex: the layout of direction and orientation domains. *Adv Exp Med Biol* 333, 57–69
42. Hanazona, G. et al. (2008) Evaluating neural activity of retinal ganglion cells by flash-evoked intrinsic signal imaging in macaque retina. *Invest ophthalmol vis sci* in press

Chapter 15
Stimulus-Induced Pairwise Interaction Can Be Revealed by Information Geometric Approach

Hiroyuki Nakahara, Masanori Shimono, Go Uchida and Manabu Tanifuji

Abstract Understanding the interaction of neural activities is one of the most important themes in neuroscience. To resolve this question, cross-covariogram analysis of two neurons' activities is one of most extensively used techniques. This analysis is conducted mostly against the null hypothesis of independent firing. Here, we argue that an additional analysis is required to understand the role of correlation with respect to behaviourally relevant parameters such as visual stimulus. Specifically, we propose conducting this analysis against the null hypothesis of the activity in a control period. We show that information geometric approach can achieve this task. Furthermore, we demonstrate the validity of this method using data taken from the inferior temporal cortex. The results indicate the possible existence of a stimulus-modulated correlation.

Keywords Pairwise interaction · correlation · information geometry · neural firing · inferior temporal cortex

Introduction

The multi-unit recordings of many neural activities have become widely available, and to make best of such massive data, methods of analysis need to be further developed. As an attempt to achieve this goal, we previously proposed information geometry (IG) approach to decipher interactions of neural firing [4]. In this paper, we illustrate this approach by focusing on the simplest case of analysis, namely an examination of cross-correlation between two neurons.

We previously noted [1] that, although cross-covariogram analysis usually examines correlated activity against the null hypothesis of no correlation, it is often more appropriate to evaluate such correlated activity against the activity in a control period. Section 'Preliminaries' clarifies this issue. The IG approach

H. Nakahara
Lab for Integrated Theoretical Neuroscience, RIKEN Brain Science Institute, 2-1 Hirosawa, Wako, Saitama, 351-0198, Japan
e-mail: hn@brain.riken.jp

R. Wang et al. (eds.), *Advances in Cognitive Neurodynamics*,

allows us to easily handle such a test, which is explained in Section 'Information Geometric-Approach'. In Sections 'Experimental Setting' and 'Results' we demonstrate the method by using real data recorded from the inferior temporal (IT) cortex. The results suggest that a stimulus-modulated correlation exists. Finally, a short discussion is given in Section 'Discussion'.

Preliminaries

Cross-Covariogram Analysis

Cross-covariogram analysis is most extensively used for analyzing the cross-correlation of a pair of two neurons. This analysis implicitly presumes wide-sense stationarity, so all of the arguments below, are made under this assumption. This analysis is mostly combined with the shuffled predictor, called the conventional cross-covariogram analysis in this paper. The shuffled predictor creates a distribution of the null hypothesis that retains the mean firing rate of each neuron but has no correlation between their firings, i.e. they are independent firings. Thus, such an analysis can only reveal whether neural firing is correlated or not within a period of interest in comparison to no correlation.

Analysis Against the Null Hypotheses of Control Period

We now propose that an equally important test is to examine whether neural firing in a period is correlated in comparison with the firing in another period.

To understand why this is important, by way of example, let us consider a single-unit recording using control and test periods. In the control period, the experimental manipulation is usually kept to a minimum, so activity in this period is regarded as being in resting mode. In the test period, some manipulations are done, e.g. showing a visual stimulus, to examine how a neuron responds to the manipulation. The firing in the test period is tested against the firing in the control period. If significant, the firing in the test period is considered test-related. Note that we would not call the firing test-related if we performed the test against zero firing, even if significance was found by that test.

The same argument can be applied to the cross-covariogram analysis. To examine whether a test-related correlation exists, we should examine the correlation in the test period against that in the control period, i.e. against the null hypothesis of the correlation in the control period, but not as done by conventional cross-covariogram analysis. Obviously, this type of argument is generalized for examining the firing between any two periods of interest.

Information-Geometric Approach

Information geometry (IG) provides useful tools and concepts, including the orthogonality of coordinate parameters and the Pythagoras relation in the

Kullback-Leibler divergence [2]. Using the IG approach, a novel method can be constructed to evaluate the interaction of neural firing in a systematic manner [1, 3]. The method allows us to decompose the interactions of neurons of various orders, e.g. pairwise, triplewise and higher order interactions [1]. It can also be applied to analyze and compare different models used for a spike train of single neurons [4]. This further allows us to construct, relatively easily, a hypothesis test under the framework of a log likelihood ratio test [1]. This generality allows us to examine a test of correlation against any null hypothesis [1].

For the cross-correlation (under wide-sense stationarity), we use the IG mixed coordinates $(\eta_1, \eta_2, \theta_3)$ (see [1] for more details). θ_3 is the term measuring the interaction. The Fisher information matrix induces a natural metric, by which we can verify the orthogonality between η and θ components. Such orthogonality cannot generally hold if we replace θ_3 by the interaction term used by the cross-covariogram analysis, denoted here by c. In fact, only when $c = 0$, i.e., there is no correlation, does the orthogonality hold between η and c, and this is why a cross-covariogram analysis is convenient only for a test of no correlation.

Experimental Setting

Experimental details are published elsewhere [5, 6], so only a brief summary is provided here. We conducted simultaneous recording of multi-unit activity from the IT cortex of two anesthetized macaque monkeys. Both control and stimulus periods had 1 sec length, where a visual stimulus is presented in the stimulus period. Correlation is estimated by the IG mixed coordinates for each period, using a 5-ms bin size. In the following, we report the results of correlation at a time lag of zero, i.e. simultaneous coincident firing.

Results

In this section, we report the results of 21 pairs of neurons, where each pair is categorized as either an R-R or R-NR pair. Here, R indicates that one neuron's firing is task-related (Wilcoxon test, $p < 0.05$), whereas NR indicates that one neuron's firing is not. We found 11 R-R pairs and 10 R-NR pairs.

First, we tried to perform a conventional cross-covariogram, for which we used the IG approach by setting the null hypothesis as $\theta_3 = 0$, since it is essentially equivalent. We found that *all* pairs had significant correlation, even in the control period, and further that almost all pairs (precisely, all except one R-NR pair) also had significant correlation in the test period. Thus, in this data, the conventional cross-covariogram is not informative for comparing the correlation between the two periods. However, if we still wanted to use this test to determine whether the correlation had changed from the control to the test period, one way might be to indicate whether the significance had changed between the above two results, i.e. Fig. 15.1 left; in this case, almost all pairs would be classified as unmodulated.

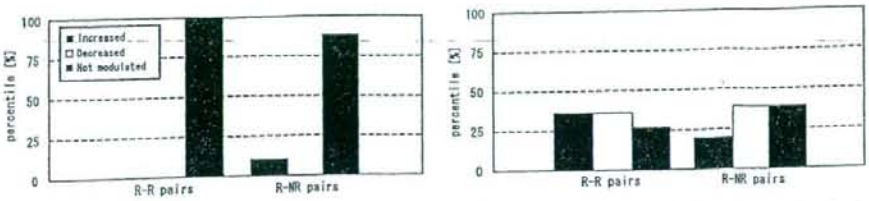

Fig. 15.1 Correlation in stimulus period is examined in comparison with that in control period, indirectly (left) or directly (right). See main text for details. Black, white, and hatched bars indicate the percentage of the number of pairs with correlation significantly increased, significantly decreased, or non-modulated, respectively

Now let us directly examine by the IG approach whether the correlation in the test period is significantly different from that in the control period (Fig. 15.1 right). We find that R-NR pairs have more decreased correlation whereas R-R pairs equally have both increased and decreased correlation. Clearly, this result is more informative in that it reveals either increased or decreased modulation for more number of pairs. It appears that the simultaneous correlation may be differentially modulated for R-R and R-NR pairs. More specifically, given the results of other analyses we performed [6], it will be particularly interesting if further analysis will lead to the observation that the correlation is increased for two neurons if both have task-related activity but decreased for two neurons if one of them does not have task-related activity. To confirm, though, we still need to examine with a greater number of samples.

Discussion

We presented one utility of the IG approach, specifically the flexible use of any null hypothesis, by using real data from the monkey IT cortex in a cross-correlation analysis. The results are promising for further investigations.

Acknowledgments We thank M. Tatsuno for his technical assistance. HN is supported by Grant-in-Aids on Priority Areas Research (C) from MEXT and for Young Scientists (A) from JSPS.

References

1. Nakahara, H., Amari, S.: Information geometric measure for neural spikes. Neural Comput. **14** (2002) 2269–2316.
2. Amari, S., Nagaoka, H.: Methods of Information Geometry. American Mathematical Society/Oxford Univ. Press, Providence (2000).
3. Nakahara, H.: Comments on analysis of neural coding by information geometric measure. International Symposium on Nonlinear Theory and its Applications, NOLTA2004, Fukuoka, Japan, Nov 29–Dec 3, 2004, Proceedings. (2004) 31–34.